

# Spectroscopic Approach to Correction and Visualisation of Bright-Field Light Transmission Microscopy Biological Data

Ganna Platonova <sup>1,2</sup> , Dalibor Štys <sup>1</sup>, Pavel Souček <sup>1</sup>, Kirill Lonhus <sup>1,2</sup>, Jan Valenta <sup>3</sup> and Renata Rychtáriková <sup>1</sup> \*

<sup>1</sup> University of South Bohemia in České Budějovice, Faculty of Fisheries and Protection of Waters, South Bohemian Research Center of Aquaculture and Biodiversity of Hydrocenoses, Institute of Complex Systems, Zámek 136, 373 33 Nové Hradky, Czech Republic; gplatonova,štys,psoucek,lonhus,rrychtarikova@frov.jcu.cz

<sup>2</sup> University of South Bohemia in České Budějovice, Faculty of Science, Branišovská 1760, 370 05 České Budějovice

<sup>3</sup> Charles University, Faculty of Mathematics and Physics, Ke Karlovu 3, Prague, Czech Republic; jan.valenta@mff.cuni.cz

\* Correspondence: rrychtarikova@frov.jcu.cz (R.R.)

**Abstract:** The most realistic information about the transparent sample such as a live cell can be obtained only using bright-field light microscopy. At high-intensity pulsing LED illumination, we captured a primary 12-bit-per-channel (bpc) response from an observed sample using a bright-field wide-field microscope equipped with a high-resolution (4872×3248) image sensor. In order to suppress data distortions originating from the light interactions with elements in the optical path, poor sensor reproduction (geometrical defects of the camera sensor and some peculiarities of sensor sensitivity), this uncompressed 12-bpc data underwent a kind of correction after simultaneous calibration of all the parts of the experimental arrangement. Moreover, the final intensities of the corrected images are proportional to the photon fluxes detected by a camera sensor. It can be visualized in 8-bpc intensity depth after the Least Information Loss compression [Lect. Notes Bioinform. **9656**, 527 (2016)].

**Keywords:** bright-field photon transmission microscope; 12-bit raw data; colorimetric calibration; least information loss conversion; videoenhanced microscopy; microscope images correction.

## 1. Introduction

Techniques of light microscopy give us a possibility to investigate features of various types of specimens and have been considered as the standard in living cells observation for decades [1–3]. However, each of these microscopic techniques suffers from some disadvantages.

Unlike transmitted and reflected light microscopy techniques, fluorescence microscopy only allows the observation of specific structures which have been preliminarily labeled for fluorescence. Other limitations of the fluorescence microscopy are connected with photobleaching [4] of applied dyes or fluorophores and their phototoxicity influence on biological processes of a live sample with time running [5,6]. These aspects are avoided in contrast microscopy, e.g., phase contrast microscopy or differential interference contrast microscopy [7], where, naturally, some intracellular structures are enhanced whereas some of them are suppressed by artificial light interferences [8]. Nevertheless, for observation of the biological experiments using all microscopic techniques mentioned above, a grayscale digital camera is sufficient [9–12].

Classical bright-field transmission microscopy allows the observation of unlabeled living cells and tissues and their internal structures and is of increasing interest due to recent experiments on super-resolution using videoenhancement [13] and live cell dynamics [14]. In order to describe the spectral properties of the observed sample, in the proposed microscope arrangement [13,14], the object response is captured by a color digital camera. As a result of even slight defects of the camera sensor and aberrations in the optical path, images may



**Citation:** Platonova, G.; Štys, D.; Souček, P.; Lonhus, K.; Valenta, J.; Rychtáriková, R. Spectroscopic Approach to Correction and Visualisation of Bright-Field Light Transmission Microscopy Biological Data. *Preprints* **2021**, *1*, 0. <https://doi.org/>

Received:

Accepted:

Published:

**Publisher's Note:** MDPI stays neutral with regard to jurisdictional claims in published maps and institutional affiliations.

suffer from strong distortions which disable an exact and simple data processing and analysis. Therefore, the microscope with the camera should be calibrated as any measurement device in order to achieve more accurate representation of the object for further digital processing or visualization.

With the growing popularity of image processing automation, the question of technically correct and accurate images becomes even more acute. Different approaches to calibration have been developed by now and are widely used in various microscopy techniques. Authors refer to the necessity of digital compensation of pixel-dependent noise specific to modern cameras used in fluorescent [15] and single molecule localization microscopy [16] as they affect the results of images analysis by software. In [17], authors introduced a theoretical model of noise sources and proposed their correction algorithm for fluorescence microscopy. On the other hand, there are approaches to pure data-driven determination of statistical properties of imaging sensors [18]. In [19], authors discuss the impact of vignetting in application to light field microscopy and introduce a calibration procedure to determine optically correct reference point for microlens-based systems. Photometric calibration in spectral microscopy is discussed in [20] where a method is proposed to compensate the non-uniform spectral response and quantum efficiency and calibrate the equipment.

In the presented article we describe a method for capturing, correction, and conversion of 12-bit raw images of unmodified biological samples obtained using a videoenhanced bright-field wide-field microscope. The image correction is based on the spectral characteristics of light captured by each camera sensor pixel during the calibration process. The advantages of the calibration method is demonstrated on both an image data visualization algorithm and simple image processing algorithms. The possible image visualization utilizes a full 8-bit-per-channel (bpc) range for transformation of corrected images (that depicted originally spatial distributions of spectral radiant fluxes). In this way, we acquired the most informative (in the sense of color and contrast) microscopic images of cells that can be mutually visually compared at the level of the whole image series. As we show further in this paper, the described method of the microscope calibration brings also benefits to the subsequent microscopy image processing and analysis.

The calibration method may be technically improved but, from the conceptual point of view, is complete.

## 2. Materials and Methods

### 2.1. High-resolution bright-field wide-field light microscope

In this paper we present the process of calibration of the optical path and digital camera sensor of a high-resolution bright-field wide-field light transmission microscope enabling observation of microscopic objects, further called the nanoscope [13,14]. This microscope was developed by the Institute of Complex Systems (ICS) of the Faculty of Fisheries and Protection of Waters (FFPW) in collaboration with the Petr Tax - Optax company (Prague, Czech Republic). The optical path consisted of two Luminus 360 light emitting diodes charged by the current up to 5000 mA. This allows the videoenhancement [21] by illumination of the sample by series of light flashes with a blinking pattern 'light for 0.2261 s–dark for 0.0969 s'. A projective lens magnifies ( $2\times$ ) and projects the image on a JAI camera with a 12-bpc color Kodak KAI-16000 image sensor of  $4872\times 3248$  image resolution. The process of capturing the primary signal is controlled by a custom control software. The optical system of the microscope is facilitated by infrared and ultraviolet filters Edmund Optics (USA). This prototype microscope allows to conduct experiments in time-lapse mode (a capturing of the image series at one focus position) and scanning of the interior of the cell along the optical axis in the z-scan mode (capturing in different z-positions). The z-scan can be performed automatically by a programmable mechanics with the step size down to the 100 nm.

Figure 6d shows an image from a time-lapse experiment on HeLa cells taken at the microscope set-up as follows: camera gain 0, offset 0, and exposure 148 ms; LED current 4500 mA; objective Nikon LWD 20 $\times$ /0.4, Ph1 ADL,  $\infty$ /1.2, WD 3.1. Figure 8 shows an image from a time-lapse experiment (737 images) on mouse fibroblasts taken at the microscope set-up as follows: camera gain 0, offset 300, and exposure 293.6 ms; LED current 4500 mA; ILCX -106  $\mu$ m; ILCY -201  $\mu$ m; objective Nikon Plan 40 $\times$ /0.65,  $\infty$ /1.17, WD 0.56. Figure 9 was acquired on the same Nikon 40 $\times$  objective as Figure 8.

The comparative biological experiments in Figure 6 were done using

1. a Nikon Eclipse 80i microscope with an objective Nikon Plan Fluor 40 $\times$ /0.75, Ph2 DLL,  $\infty$ /0.17 WD 0.66 and a CCD-13QB camera and
2. an Olympus IX51 microscope with an objective LUC Plan FLN 40 $\times$  0.60 Ph2,  $\infty$ /0-2/NF 22 and an Infinity 1 camera.

Both these commercial microscopes are placed in the Tissue Culture Workplace at the ICS FFPW.

## 2.2. Microscope system calibration and image correction

The microscope system that was calibrated is the nanoscope (see Section 2.1). The optical fiber spectrometer used for the calibration of the microscope system was calibrated itself by the procedure described in Appendix A. The scheme of the measuring apparatus is seen in Figure 1.

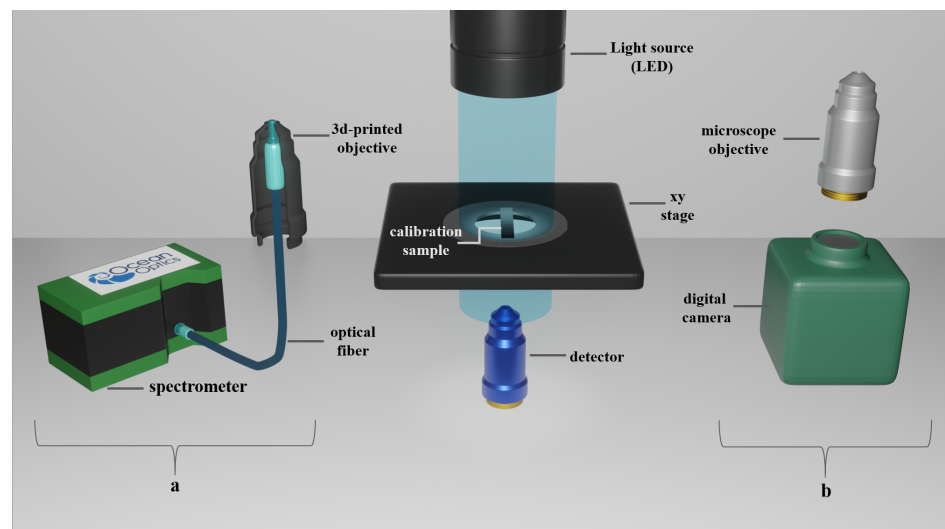


**Figure 1.** The scheme of the measuring apparatus for calibration of the light microscope. a) Fiber of the optical spectrophotometer placed into the plastic imitation of the microscope objective – arrangement for measurement of the microscope light source spectra after passing through the grayscale calibration filters. b) A real microscope objective and a digital camera as the main part of the arrangement for acquisition of the calibration digital images of the grayscale calibration filters.

The camera calibration and image correction was performed in the steps as follows:

1. Focus position determination.
  - (a) During an image acquisition, a light is passing through the microscope optical path and sample. The resulted signal is then captured by a camera sensor. A Linear Step ND Filter NDL-10S-4 (Thorlabs, USA) was used for the light attenuation with 11 different grades. The filter itself is a thin layer of light absorbing

material coated on one side of a 2 mm reference glass. Filters 5–11 (counted from the darkest one) were scanned through their whole depths with the step of 100 nm. Results for filter F12 were obtained for a path of ray without any filter. In this way, 8 sets of 1309 images each were obtained.

- (b) These 8 sets of images were processed by Image Info Extractor Professional software (ICS FFPW) (chosen Rényi parameter  $\alpha = 2$ ) [22]. The point information gain entropy (PIE) gives a total change of the image information after iterative removing of one pixel from an individual image. The highest value of this parameter allows to pick an in-focus image taken from the center of the coatings (Figure 2). This reduced the diffraction-induced aberrations from the boundaries of the calibration sample.

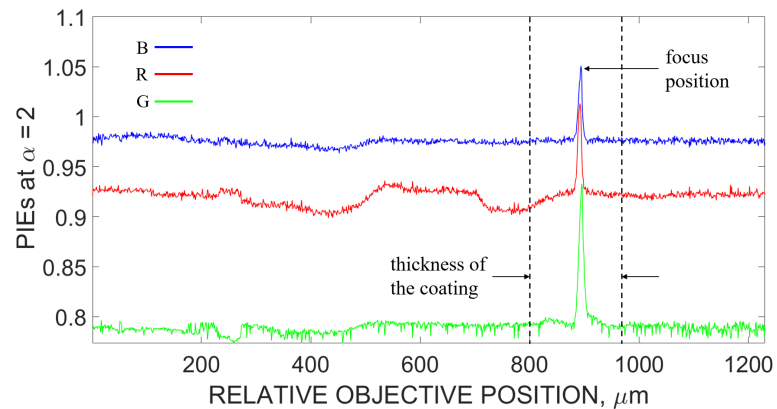


**Figure 2.** The dependence of the PIE at  $\alpha = 2$  on the relative position of the objective along the z-axis for the red (R), green (G), and blue (B) channel of a calibration gray filter (F8 opacity). The z-positions correspond to the images' orders. The in-focus image that was selected for the microscope calibration is shown by the arrow. The used microscope objective was a Nikon Plan 40 $\times$ /0.65,  $\infty$ /0.17, WD 0.56 at LED current 4500 mA.

2. Acquisition of calibration images and transmission spectra of calibration grayscale filters.
  - (a) A set of calibration data (40 images for each calibration coating) was taken at the determined focus position (see item 1b). The calibration images were calculated as a pixel-wise mean through the image sets corresponding to each of the coatings. In such a way we reduced a random noise in the measured data.
  - (b) An optical waveguide P400-1-UV-VIS was placed inside a 3D-printed microscope objective at the determined focus position and connected to a spectrometer Ocean Optics USB 4000 VIS-NIR-ES. The spectral responses F5–F11 in Figure 3c correspond to gray filter coatings of the 5th–11th opacities. The spectral response F12 reflects electroluminescence captured without any filter coating by a microscope camera during exposure.
3. Calculation of the radiant fluxes reaching each microscope camera pixel after passing the gray calibration coatings.
  - (a) The raw microscope diode wavelength-dependent signal obtained by a spectrophotometer (Figure 3c) was divided by a spectrophotometer sensitivity wavelength-dependent curve (Figure 3b). That gave the final calibrated microscope diode signal (Figure 3d).
  - (b) After data smoothing and interpolation, the light spectra reaching each pixel of the camera sensor (Figure 3e) were obtained as multiplication of the incoming

spectra (measured by the calibrated spectrometer; see item 3a and Figure 3d) by the respective (red, green, blue) quantum efficiency profile of the Kodak KAI-16000 image sensor (Figure 3a).

- (c) For each gray filter coating, the radiant flux (Figure 3f) reaching each pixel during exposure were calculated as an integral (trapezoidal rule) of the area below the respective incident spectrum.
4. Calibration curves and image correction.
    - (a) Calibration curves were obtained for each image pixel position and respective extend of values of camera channel radiant flux (see the range of filter coatings in items 1–2). The calibration curves map the pixel intensities to the real spectra responds (e.g., Figure 4). Linear interpolation was used for intermediate points.
    - (b) In order to extent the range of experimental (useful) intensities, the initial calibration curves for each pixel were extrapolated linearly about 80% (Figure 4, magenta line). Statistics of the pixels' intensity values for every calibration filter were evaluated (Figure 5) in order to see the deviations of the sensor responses from idealities.
    - (c) Hereafter, the calibrated image format (in double precision numbers showing the spatial distribution of radiant fluxes in a microscopy image) was transformed to a png format. The calibration curve associates the value of each calibration intensity with the respective experimental measured photon energy.

The computation part of the microscope system calibration and image correction described in items 3b,c and 4 is implemented in the software VerCa (ICS FFPW).

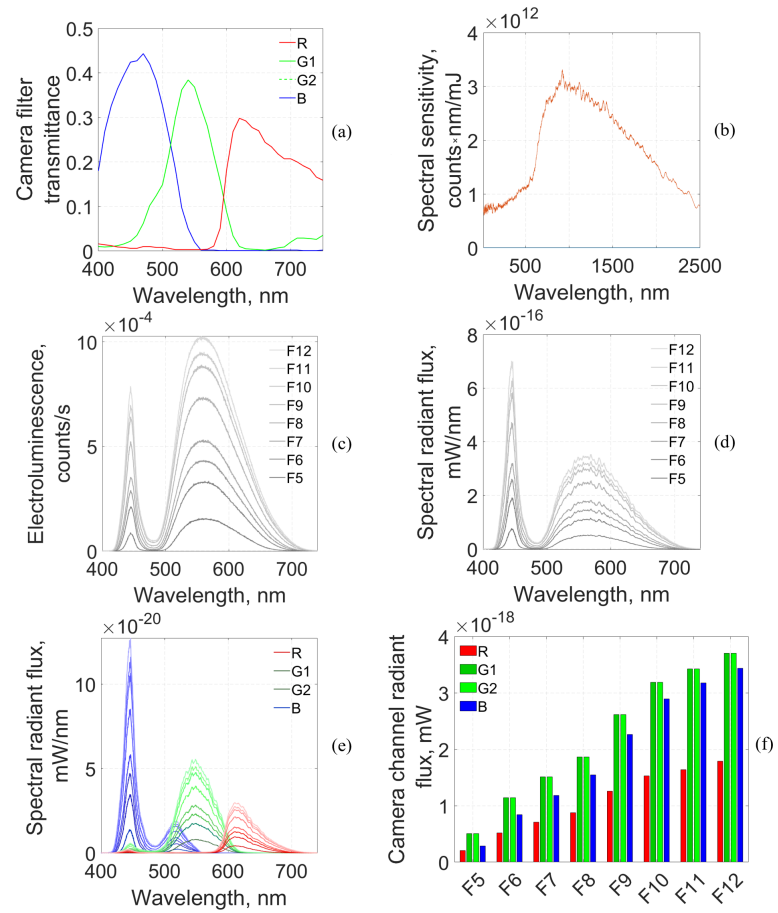


**Figure 3.** a) The declared spectra of the Bayer mask filters for a Kodak KAI-16000 camera sensor. b) The response of the Ocean Optics USB 4000 VIS-NIR-ES spectrometer with a fibre P400-1-UV-VIS after illumination by a NIST calibrated lamp. c) The light spectra of gray filter coatings NDL-10S-4 measured by a fiber spectrometer, opacities of the calibration filter is decreasing with increasing of the calibration filter number (F5–F12). d) Incoming light spectra corrected to the fiber spectrophotometer spectral sensitivity. e) The spectra of incoming light captured by the red (R), green (G1, G2) and blue (B) camera pixel. f) Integral spectral values (radiant fluxes) reaching red, green, and blue camera pixels, respectively, after passing each individual calibration coating F5–F12.

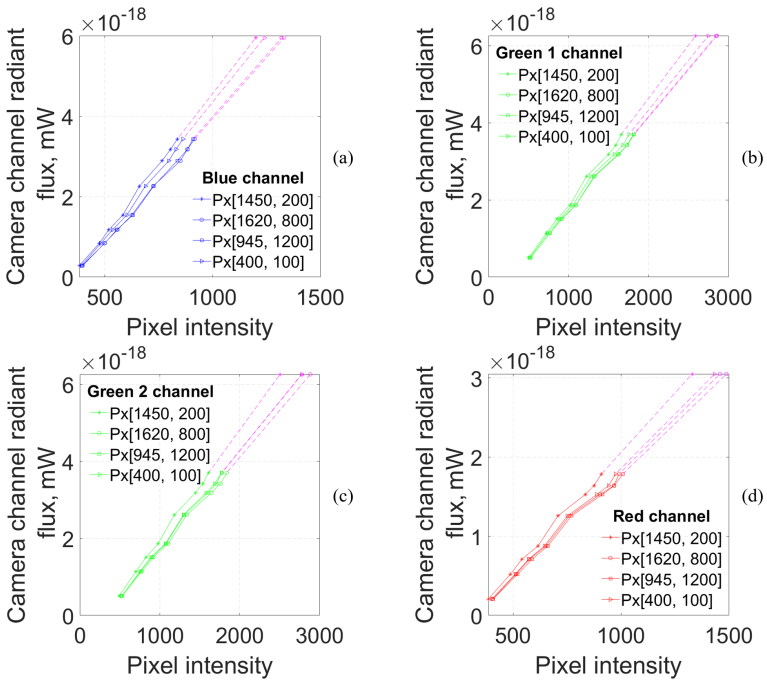


**Figure 4.** Exemplary calibration curves for the blue (a), green 1 (b), green 2 (c), and red (d) camera pixels [1450, 200], [1620, 800], [945, 1200], and [400, 100] (counted after image debayerization) for a microscope objective Nikon Plan 40×/0.65, ∞/0.17, WD 0.56 (LED current 4500 mA, ILCX -106 μm, ILCY -201 μm).

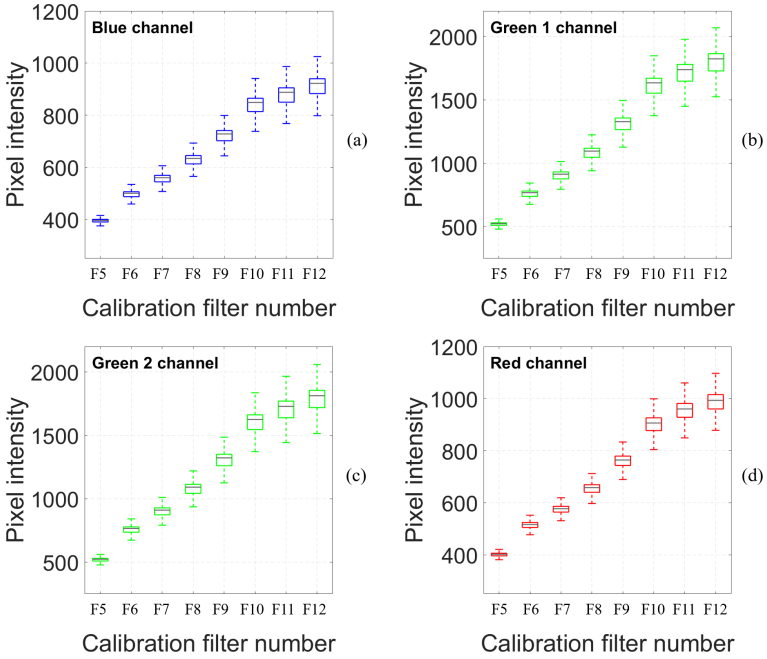


**Figure 5.** Distributions of the calibration image intensities corresponding to Figure 4.

2.3. Least information loss (LIL) image conversion

The resulted calibrated images have >8-bpc png format, but nowadays majority of digital screens can show only 8-bpc formats. For practical purpose the LIL Converter software was

developed by the ICS FFPW. It converts  $>8$ -bpc images more informatively and comparably [23]. This program allows to convert RGB, grayscale, and raw (an appropriate Bayer mask [24] can be selected) data format to 8-bpc images. Rescaling the intensities in each color (r, g, or b) channel can be applied for image sets of any length (even for one image only) either separately (when the intensity maximum and minimum is found for each color channel separately) or together (one common intensity minimum and maximum, respectively, is found for all color channel together). If color channels are normalized separately, more information in the image is preserved. In case of multi-image series, the intensities are rescaled between intensity maximum and minimum through the whole series. The empty (unoccupied) levels are always removed in case that they are empty in all images of the image set. The basic LIL algorithm is written in Appendix B.

The images can be cropped which is useful namely for removing dead pixel's rows and columns. Intensities of, e.g., dead or hot pixels can be eliminated in the image by a thresholding function that, before applying the LIL conversion, replaces the undesirable intensities in an original vice-bit image by a neighbor pixel's active intensity. The program is optimized to utilize multi-core CPUs.

### 3. Results and Discussion

The nanoscope described in Section 2.1 was developed mainly for studying unlabeled live and fixed cells to investigate the sample real structures. It means that any (immuno)fluorescent modifications are not applied to the cells and no additional contributions to the object response influence the detected signals. Investigation of the unmodified samples does not require complicated sample preparation and does not decrease the lifetime of the living cells.

In Figure 6, HeLa cells are presented in the bright-field, phase contrast, and a fluorescent mode of a commercial microscope and in videoenhanced high-resolution imaging using the nanoscope at the same magnification. The staining for fluorescence microscopy (Figure 6c) visualizes only selected parts of the cell. Interior and information about the positions, shapes, or behavior of other organelles is lost. In the phase contrast imaging (Figure 6a), the cell borders are surrounded by halos of light interference. In the bright-field mode of the commercial microscope (Figure 6b), the cell structures are hardly observed mainly due to a lower intensity of illumination and a larger size of an object which can be projected on a camera pixel. Moreover, due to the usage of a grayscale camera, the spectral characteristics of the standard bright-field image are hardly analyzable. In contrast, the nanoscope (Figure 6d) provides primary color images where all cell borders, nucleus, nucleolus, condensing chromosome during mitosis, and some other organelles are nicely visible and the contrast can be further intensified by the method of simultaneous optical path and camera chip calibration applied to the primary, raw, camera signal (Section 2.2).

The proposed calibration method (Section 2.2) allows to obtain more realistic spectral properties of a microobject. Even in absence of the sample, the incoming light is distorted by the optical path and non-idealities of the camera sensor. Our method helps to mitigate such problems, improving any consecutive method of analysis. It is shown in Figure 7b that after data correction the image histograms have narrower range of intensities than those before the correction (Figure 7a). Moreover, the calibrated image shows no signs of optical vignetting (which is undesirable mainly for macroscopic camera imaging purposes; the fields of view of most microscopes are too small to show the edge optical vignetting).

For the correct assessment of experimental results, a proper visualization of the  $>8$ -bpc images is important as well. For this, we proposed a LIL algorithm (Section 2.3). Figure 8 shows images of mouse fibroblasts with and without prior calibration converted using the LIL algorithm applied to a single image and a whole time-lapse series. Figure 7c–f further presents intensity histograms relevant to the images in Figure 8. There is a visible vertical line in the



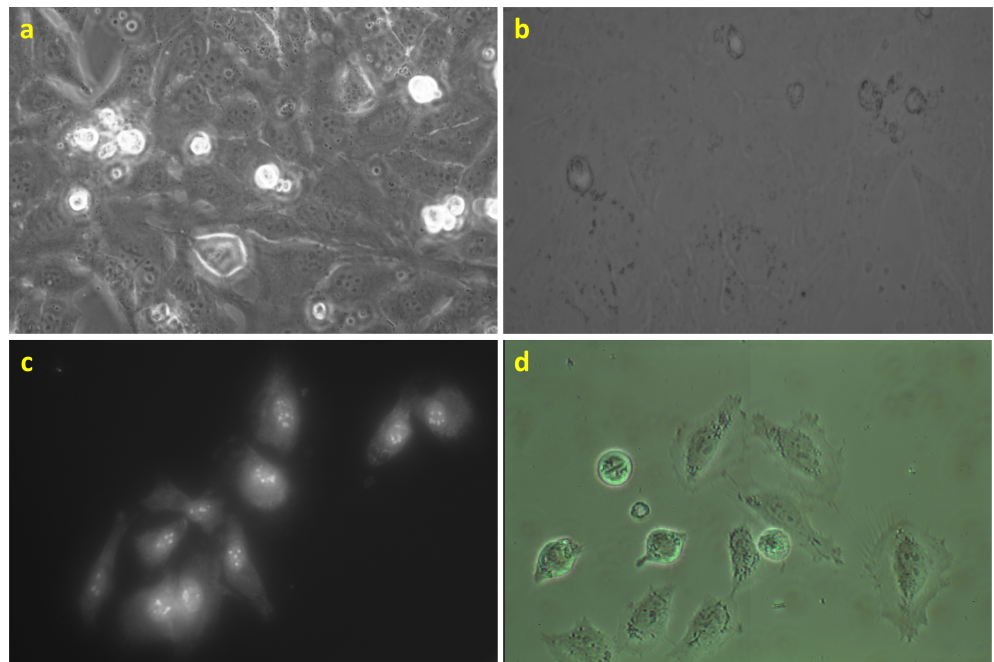


**Figure 6.** 8-bit images of HeLa cells pictured by a) a phase contrast microscope Olympus IX51 with an Infinity 1 camera (40 $\times$  objective magnification), b) a bright-field microscope Olympus IX51 with an Infinity 1 camera (40 $\times$  objective magnification) giving raw image data and c) a fluorescent microscope Nikon Eclipse 80i in its standard arrangement (40 $\times$  objective magnification, stained by fluorescein), and d) the nanoscope (20 $\times$  objective magnification followed by 2 $\times$  projective lens magnification) giving raw image data (without microscope calibration). Panels b and d are visualized by the LIL algorithm.

middle of every uncalibrated image. It is caused by sensor taps' imbalance problem, which can be crucial for digital processing algorithms. In addition, in the corrected image we suppressed artifacts such as grains of dust in the microscope optical path (cf. Figure 8a with c) and intensified color contrast between different cellular structures and the background. All images in Figure 8 were obtained by the separate normalization of color channels and thus there are no natural colors. Even though the information is necessarily lost in the transformation from >8-bpc into 8-bpc images, the LIL transformation of an individual image preserves the highest proportion of it and the transformation of a whole series preserves most of the information in the series and allows a mutual visual comparison of its images.

As an example how the described method affects the subsequent image processing, we applied standard Matlab grayscale and binarization functions to the corrected and uncorrected images (Figure 9). When compared to the corrected images (Figure 9b,d), the uncorrected rgb and grayscale images (Figure 9a,c) have background non-uniformities (scratches and dust in the microscope optical path) and presents also less sharper borders of pseudopodia. The binarized images also show the improvements made by the calibration approach. We can see that small artifacts have disappeared and cells' features have become sharper and more compact in the corrected image (cf. Figure 9e and f).

#### 4. Conclusions

Biological experiments are hardly reproducible and repeatable but also often sensitive to the technical provision. The approach presented in this article allows without any extensive technical treatment to reduce, for one thing, the impact of optical path inhomogeneities and, for another thing, defects of a camera sensor on color properties of images in a bright-field light transmission microscopy experiment. Thus, it allows to maximize the yield of information obtained in the technically simplest possible experiment. The calibration procedure proposed here (if needed, followed by a correct image intensity compression) is promising for more adequate and precise transfer of color information to the computer and researchers. This experimental technology allows observation of living cells in dynamics and makes the following microscopy image processing (especially, cells' feature and edge detection) easier.

The information in the uncalibrated image is obviously dominated by the sensor and light path inhomogeneities and for proper evaluation only calibrated images may be used for assessment. This is particularly important for eventual automatic machine analysis which will be unavoidable in case of a large field of view containing many individual objects that cannot be analyzed manually.

This method allows to make easier edge detection (extraction of the edge features) which is important in image processing. It allows to do them more implicit from background of bright-field wide-field transmission image.

Nevertheless, the described image calibration and correction method is not applicable only for observation of a live cell but also for analysis of different chemical materials and structures. After some slight changes in the experimental protocol and system arrangement, the method can be also usable in light reflection or fluorescence microscopy.

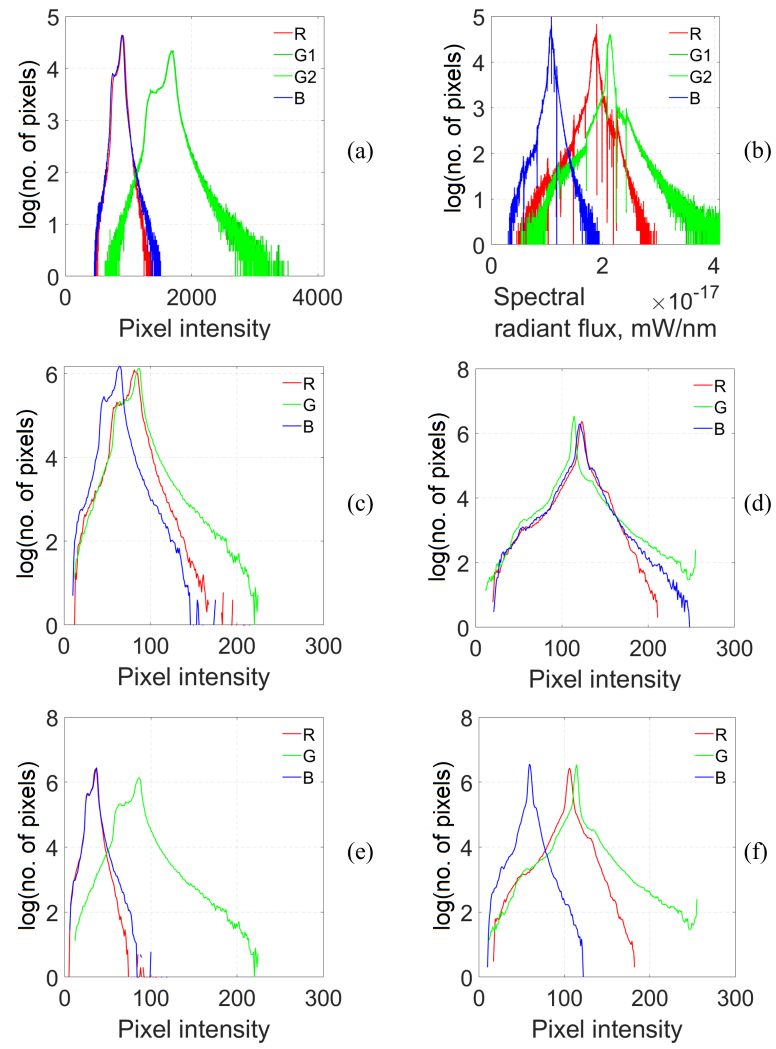


**Figure 7.** Red, green, and blue intensity histograms for raw and compressed image in Figure 8. a) Uncorrected raw image, b) spectrally corrected raw image, c) uncorrected RGB image after LIL compression of the single image Figure 8a, d) spectrally corrected RGB image after LIL compression of the single image Figure 8c, e) uncorrected RGB image Figure 8b after LIL compression through the whole image series, f) spectrally corrected RGB image Figure 8d after LIL compression through the whole image series.

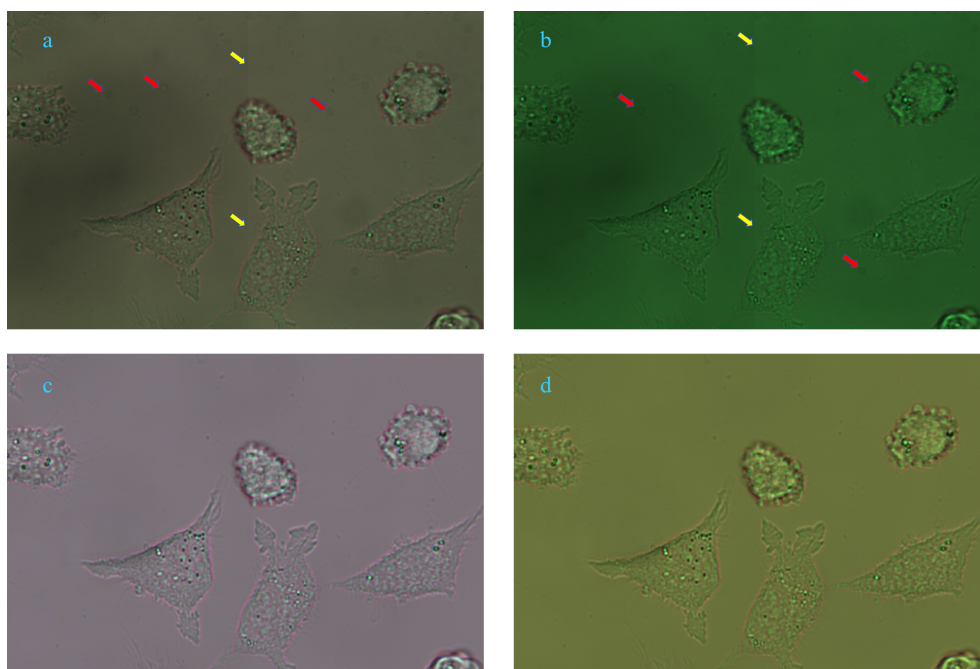


**Figure 8.** The LIL 8-bpc visualization of the original 12-bpc uncalibrated (a–b) and spectrally calibrated (c–d) image of mouse fibroblasts captured by the nanoscope ( $40\times$  objective magnification). The LIL transformation was performed for a single image (a, c) and through the whole image series (b, d). The yellow and red arrows point the sensor tap imbalance problem and stains of dirty on the microscope optics, respectively. The relevant histograms are shown in Figure 7.

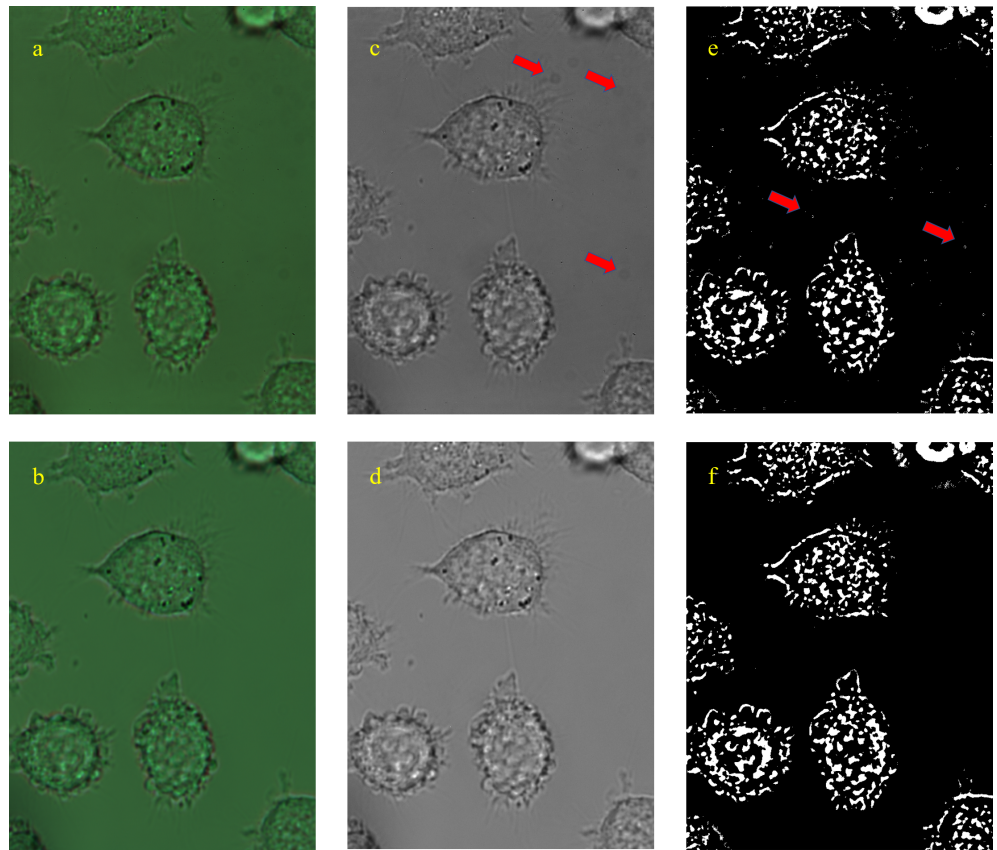


**Figure 9.** Conversions of a mouse fibroblasts' image using simple Matlab functions. a) 12-bpc original uncorrected rgb image and b) spectrally corrected image. c) Uncorrected image a after conversion to grayscale. d) Spectrally corrected image b after conversion to grayscale. e) Uncorrected image a after binarization and f) spectrally corrected image b after binarization.

**1 Author Contributions:** Conceptualization, G.P., D.Š. and R.R.; methodology, D.Š. and R.R.; software, P.S. and K.L.; validation, G.P., D.Š. and R.R.; formal analysis, G.P., D.Š. R.R.; investigation, G.P., D.Š. R.R. and J.V.; resources, D.Š.; data curation, G.P.; writing—original draft preparation, G.P.; writing—review and editing, R.R.; visualization, G.P.; supervision, D.Š. and R.R.; funding acquisition, D.Š. All authors have read and agreed to the published version of the manuscript.

**6 Data Availability Statement:** The supplementary data, namely Figures 2, 4, 5, and 9 at other microscope set-ups, calibration sets, and Matlab scripts are available at [26].

**8 Funding:** This work was supported by the Ministry of Education, Youth and Sports of the Czech Republic – projects CENAKVA (LM2018099) and from the European Regional Development Fund in frame of the project Image Headstart (ATCZ215) in the Interreg V-A Austria–Czech Republic programme. The work was further financed by the project GAJU 017/2016/Z. One of the authors (J.V.) acknowledges funding form the Charles University centre UNCE/SCI/010.

**13 Acknowledgments:** The authors would like to thank Petr Macháček (ImageCode, Brloh, CZ), Ali Ghaznavi, and Vladyslav Bozhynov (both from ICS USB) for their support to this paper.

**15 Conflicts of Interest:** The authors declare no conflict of interest. The funders had no role in the design of the study; in the collection, analyses, or interpretation of data; in the writing of the manuscript, or in the decision to publish the results.

## 18 Abbreviations

19 The following abbreviations are used in this manuscript:

20 LED	light-emitting diode
bpc	bits per channel
ICS	Institute of Complex Systems
ILCX	x-position read out by a microscope incremental linear sensor
ILCY	y-position read out by a microscope incremental linear sensor
FFPW	Faculty of Fisheries and Protection of Waters
N.A.	Numerical Aperture
21 ND	Neutral Density
PIE	Point Information Gain Entropy
PIG	Point Information Gain
VIS-NIR-ES	visible and near-infrared with enhanced sensitivity
LIL	Least Information Loss algorithm
LWD	microscope objective low working distance
NIST	National Institute of Standards and Technology
WD	microscope objective working distanc

## 22 Appendix A Optical fiber spectrophotometer calibration

23 A new tungsten-halogen calibration lamp (a NIST standard of spectral irradiance) Oriel  
24 Mod. 63358, S/N:30024 with a power supply Oriel OPS-Q250 (stabilized at 6.5 A for more  
25 than 1 h) was used as a calibration standard. The calibrated device was a spectrometer Ocean  
26 Optics USB4000-VIS-NIR-ES (S/N USB4U06341) with a fibre P400-1-UV-VIS (1 m long, 0.4  
27 mm core, SMA connectors). The distance between the lamp and the entrance of the calibrated  
28 system (fibre input) was 50 cm. For the measurements, the parameters of spectrophotometer  
29 control software Ocean View was set up as follows: Time 30 ms, Electric dark OFF, Scans to  
30 average 3. The signal was above half of the full range (which is a 16-bit number). The dark  
31 signal was measured separately (Figure A1).

32 From the experimental data, the net signal rate [count·s<sup>-1</sup>] was calculated as  $NSR = \frac{\text{light signal} - \text{dark signal}}{0.03}$ . This was divided by the lamp spectral irradiance (the calibration  
33 provided by the NIST for 50 cm distance gives in the visible spectral region 400–800 nm  
34

35 a monotonously increasing function from about  $0.43$  to  $7.56 \text{ mW}\cdot\text{cm}^{-2}\cdot\text{nm}^{-1}$ ) multiplied  
36 by a fibre core area ( $1.25\times 10^{-3} \text{ cm}^2$ ). This gives an input spectral power [ $\text{mW}\cdot\text{nm}^{-1}$ ]. The  
37 resulted value is the system response (or sensitivity, Fig. 2b) in [ $\text{count}\cdot\text{nm}\cdot\text{mW}^{-1}\cdot\text{s}^{-1}$ ] =  
38 [ $\text{count}\cdot\text{nm}\cdot\text{mJ}^{-1}$ ]. The reflection of light on the fibre-air interface is not corrected for as it is  
39 part of the system response.

40 Several measurements with bandpass filters were performed in order to get information  
41 on stray light effects of the spectrophotometer (they are relatively low) and the final response  
42 is corrected for it.

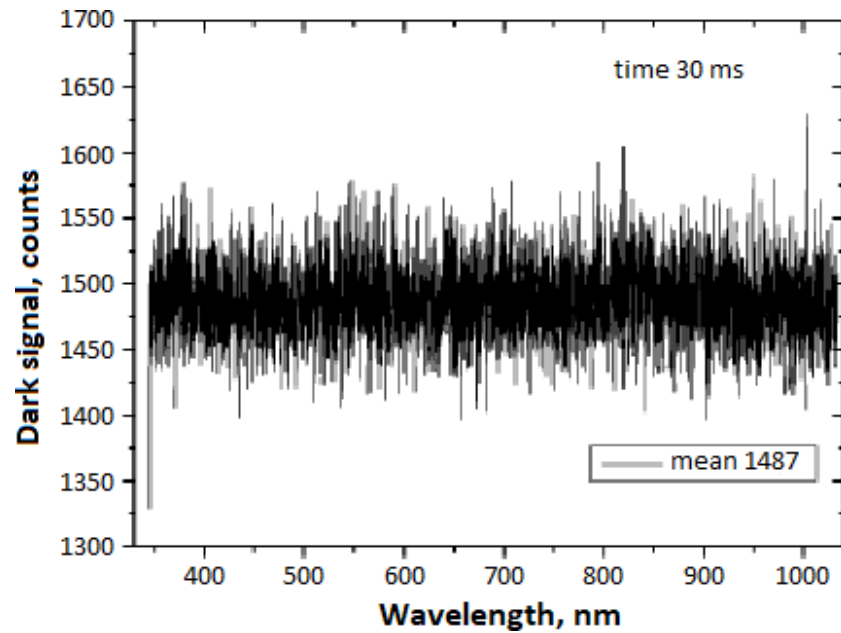


Figure A1. Dark signal of the spectrometer Ocean Optics USB4000-VIS-NIR-ES.

43 **Appendix B Least Information Loss Matlab algorithm and pseudocode**

---

**Input:** a set of  $N$  input  $n$ -bit grayscale images, where  $n > 8$ ;  
**Output:**  $\mathbf{I8}$  as a Least Information Loss transformed image of the image  $\mathbf{In}$

```

1  $\mathbf{H} = \text{zeros}(2^n, 1)$ ;      % create an empty (zero) vector of the length  $n$ 
2 for  $i = 1$  to  $N$  do
3   |  $\mathbf{In} = \text{readIm}(i)$ ;      % read an  $i$ -th  $n$ -bit image
4   |  $\mathbf{h} = \text{createHist}(\mathbf{In})$ ; % create the image  $n$ -bit histogram  $\mathbf{h}$ ;
5   |  $\mathbf{H} = \mathbf{H} + \mathbf{h}$ ;      % create the series histogram  $\mathbf{H}$ ;
6 end
7  $\mathbf{OccL} = \text{findOccLev}(\mathbf{H})$ ;
8   % write positions of all occupied intensity levels in histogram  $\mathbf{H}$ ; omit positions of
9   % the empty histogram bins;
10  $\text{NoOfOccL} = \text{length}(\mathbf{OccL})$ ;
11   % calculate the number of the occupied intensity levels  $\mathbf{OccL}$  in the series
12   % histogram  $\mathbf{H}$ ;
13  $\text{sf} = (\text{NoOfOccL} - 1) / 255$ ;
14   % compute a scale factor  $\text{sf}$  which says how many occupied levels of an image  $\mathbf{In}$ 
15   % will fall in a single, 8-bit-image, intensity; use the floor function;
16  $\mathbf{In} = \text{readIm}(j)$ ;      % read an  $j$ -th  $n$ -bit image, where  $j \in [1, N]$ 
17  $\mathbf{I8} = \mathbf{In} .* 0$ ;      % create a zero matrix of the size of image  $\mathbf{In}$ 
18  $\text{intst} = 0$ ;
19 for  $i = \text{sf}$  to  $\text{NoOfOccL}$  by  $\text{sf}$  do
20   |  $\mathbf{I8}(\mathbf{In} == \mathbf{OccL}(i) - 1) \leftarrow \text{intst} / \text{sf}$ ;
21   | % write intensity  $\text{intst} \in [1, 255]$  at the position of the image  $\mathbf{I8}$  which
22   | % corresponds to the positions in image  $\mathbf{In}$  with intensities that are higher than
23   | % intensity at the position  $i$  in the vector  $\mathbf{OccL}$ 
24   |  $\text{intst} = \text{intst} + 1$ ;
25 end

```

**Algorithm 1:** The Least Information Loss algorithm for a grayscale image.



## References

1. Stephens, D.J.; Allan, V.J. Light microscopy techniques for live cell imaging. *Science* **2003**, *300*(5616), 82–86.
2. Hell, S.W. Nanoscopy with focused light (Nobel lecture). *Angew. Chem.* **2015**, *54*(28), 8054–8066.
3. Koike-Tani, M.; Tani, T.; Mehta, S.B.; Verma, A.; Oldenbourg, R. Polarized light microscopy in reproductive and developmental biology. *Mol. Reprod. Dev.* **2015**, *80*(7–8), 548–562.
4. Fadero, T.C.; Gerbich, T.M.; Rana, K.; Suzuki, A.; DiSalvo, M.; Schaefer, K.N.; Heppert, J.K.; Boothby, T.C.; Goldstein, B.; Peifer, M.; Allbritton, N.L.; Gladfelter, A.S.; Maddox, A.S.; Maddox, P.S. LITE microscopy: Tilted light-sheet excitation of model organisms offers high resolution and low photobleaching. *J. Cell Biol.* **2018**, *217*(5), 1869–1882.
5. Icha, J.; Weber, M.; Waters, J.C.; Norden, C. Phototoxicity in live fluorescence microscopy, and how to avoid it. *Bioessays* **2017**, *39*(8), 1700003.
6. Laissue, P.P.; Alghamdi, R.A.; Tomancak, P.; Reynaud, E.G.; Shroff, H. Assessing phototoxicity in live fluorescence imaging. *Nat. Methods* **2017**, *14*, 657–661.
7. Cremer, C.; Masters, B.R. Resolution enhancement techniques in microscopy. *Eur. Phys. J. H* **2013**, *38*(3), 281–344.
8. Charwata, V.; Schütze, K.; Holthöner, W.; Lavrentieva, A.; Gangnus, R.; Hofbauer, P.; Hoffmann, C.; Angres, B.; Kasper, C. Potential and limitations of microscopy and Raman spectroscopy for live-cell analysis of 3D cell cultures. *J. Biotechnol.* **2015**, *205*, 70–81.
9. Bierbaum, M.; Leahy, B.D.; Alemi, A.A.; Cohen, I.; Sethna, J.P. Light microscopy at maximal precision. *Phys. Rev. X* **2017**, *7*(4), 041007.
10. Mignard-Debise, L.; Ihrke, I. Light-field microscopy with a consumer light-field camera. International Conference on 3D Vision, Lyon, France, 19–22 Oct. 2015.
11. Daetwyler, S.; Huisken, J. Fast fluorescence microscopy with light sheets. *Biol. Bull.*, **2016** *231*(1), 14–25.
12. Li, J.; Beaulieu, D.R.; Paudel, H.; Barankov, R.; Bifano, T.G.; Mertz, J. Conjugate adaptive optics in widefield microscopy with an extended-source wavefront sensor. *Optica* **2015**, *2*(8), 682–688.
13. Rychtáriková, R.; Náhlík, T.; Shi, K.; Malakhova, D.; Macháček, P.; Smaha, R.; Urban, J.; Štys, D. Super-resolved 3-D imaging of live cells' organelles from bright-field photon transmission micrographs, *Ultramicroscopy* **2017**, *179*, 1–14.
14. Rychtáriková, R.; Štys, D. Observation of dynamics inside an unlabeled live cell using a bright-field photon microscopy: Evaluation of organelles' trajectories. In IWBBIO2017: International Work-Conference on Bioinformatics and Biomedical Engineering; Rojas, I., Ortuño, F., Eds.; Springer: Cham, Switzerland, 2017; pp. 700–711.
15. Mandracchia, B.; Hua, X.; Guo, C.; Jia, S. Automatic correction of pixel-dependent noise: towards the ideal sCMOS camera. *Novel Techniques in Microscopy*, pp. JW4C-8. Optical Society of America, 2019.
16. Babcock, H.P.; Huang, F.; Speer, C.M. Correcting artifacts in single molecule localization microscopy analysis arising from pixel quantum efficiency differences in sCMOS cameras. *Sci. Rep.* **2019**, *9*(1), 1–10.
17. Mandracchia, B.; Hua, X.; Guo, C.; Son, J.; Urner, T.; Jia, S. Fast and accurate sCMOS noise correction for fluorescence microscopy. *Nat. Commun.* **2020**, *11*(1), 1–12.
18. Afanasyev, P.; Ravelli, R.B.; Matadeen, R.; De Carlo, S.; Van Duinen, G.; Alewijnse, B.; Peters, P.J.; Abrahams, J.P.; Portugal, R.V.; Schatz, M.; Van Heel, M. A posteriori correction of camera characteristics from large image data sets. *Sci. Rep.* **2015**, *5*(1), 1–9.
19. Mignard-Debise, L.; Ihrke, I. A vignetting model for light field cameras with an application to light field microscopy. *IEEE Trans. Comput. Imaging* **2019**, *5*(4), 585–595.
20. Thigpen, J.; Merchant, F.A.; Shah, S.K. Photometric calibration for quantitative spectral microscopy under transmitted illumination. *J. Microsc.* **2010**, *239*(3), 200–214.
21. Lichtscheidl, I.K.; Foissner, I. Video microscopy of dynamic plant cell organelles: principles of the technique and practical application. *J. Microsc. Oxford* **1996**, *181*, 117–128.
22. Rychtáriková, R.; Korbelt, J.; Macháček, P.; Císař, P.; Urban, J.; Štys, D. Point information gain and multidimensional data analysis. *Entropy* **2016**, *18*(10), 372.
23. Štys, D.; Náhlík, T.; Macháček, P.; Rychtáriková, R.; Saberioon, M. Least Information Loss (LIL) conversion of digital images and lessons learned for scientific image inspection. In Proceedings of the International Conference on Bioinformatics and Biomedical Engineering, Granada, Spain, 20–22 April 2016; Rojas, I., Ortuño, F., Eds.; Springer: Cham, Switzerland, 2016; pp. 527–536.
24. Bayer B.E. Color imaging array. Patent US3971065 A, July 1976.
25. Rychtáriková, R.; Náhlík, T.; Smaha, R.; Urban, J.; Štys, D. Jr.; Císař, P.; Štys, D. Multifractality in imaging: Application of information entropy for observation of inner dynamics inside of an unlabeled living cell in bright-field microscopy. In ISCS14: Interdisciplinary Symposium on Complex Systems; Sanayei, A., Zelinka, I., Rössler, O.E., Eds.; Springer: Berlin/Heidelberg, Germany, 2015; pp. 261–267.
26. Platonova, G.; Štys, D.; Souček, P.; Lonhus, K.; Valenta, J.; Rychtáriková, R. Data from: Spectroscopic approach to correction and visualisation of bright-field light transmission microscopy biological data. Dryad, Dataset, <https://doi.org/10.5061/dryad.63xsj3v2d>.